Analysis of CMIP6 atmospheric moisture fluxes and the implications for projections of future change in mean and heavy rainfall

Ian G. Watterson[1], Richard J. Keane[2], Martin Dix[1], Tilo Ziehn[1], Timothy Andrews[3] and Yongming Tang[3]

[1]Climate Science Centre, CSIRO Oceans and Atmosphere, Aspendale, Victoria, Australia

[2]MetOffice, Exeter, UK and School of Earth and Environment, University of Leeds, UK

[3]MetOffice Hadley Centre, Exeter, UK

23 June 2020

International Journal of Climatology

Accepted for publication 25 July 2020

Corresponding Author: Ian G. Watterson, Climate Science Centre, CSIRO Oceans and Atmosphere, Private Bag 1, Aspendale, Victoria 3195, Australia

E-mail : ian.watterson@csiro.au

Abstract

Motivated by the wide range of projections of regional rainfall (or precipitation, pr) based on the CMIP5 ensemble of global climate models, we investigate the atmospheric moisture budget of idealized rising-CO_2 (1pctCO2) simulations from ten models submitted to CMIP6. We use the new CMIP6 standard variables, the vertically-integrated eastward and northward moisture flux, and provide a multi-model assessment of these, their convergence (conv), along with water vapour path (prw). Seasonal climatologies of a 20-year base climate for pr, prw, flux, and conv match well those from the ERA5 reanalysis. In addition, composites 'H' of quantities for months in the top decile of monthly rainfall, calculated at each model grid point, produce a field of heavy rainfall, on average double that of the mean. Spatial correlation coefficients (*r*) between the pr and conv fields are typically 0.7 in each season. This rises to 0.9 for the corresponding H fields, due to the important link between moisture convergence and heavy rainfall.

Fields of standardized change (Δ), or change per degree of global warming, were calculated. The ensemble-mean Δpr is only weakly correlated with the base climate pr, and likewise for conv. However, the prw change is highly correlated with the base prw, pointing to the importance of the 'thermodynamic' change in that variable. Globally, the net Δconv is highly correlated with Δpr, around 0.9. This rises to 0.95 for the heavy-rain composites. Relationships between changes in pr and other components hold at grid points also, when the individual model results are correlated. Clearly, there is a dependence in the change in pr with that in conv, particularly for heavy rainfall. Assessment of a larger ensemble from CMIP6, using the new flux variables, would improve the evaluation of these processes, and potentially allow more confident projections in future rainfall changes.

Key words: Atmospheric moisture transport, heavy precipitation, climate change

1. INTRODUCTION

Projections for potential future change in precipitation throughout the globe have been provided by the Intergovernmental Panel on Climate Change, through chapters of its Assessment Reports, such as that by Collins et al. (2013). Current national assessments of future change under various scenarios of rising greenhouse gas concentrations include those for the UK (Murphy et al., 2018) and Australia (CSIRO and Bureau of Meteorology, 2015). The basic evidence for change from many of these assessments comes from numerical climate simulations contributed to the World Climate Research Program's Coupled Model Intercomparison Projects, with CMIP5 (see www.wcrp-climate.org/wgcm-cmip/wgcm-cmip5) being that most recently completed. These are often supplemented by regional 'downscaling' simulations, for example in the projections for eastern Australian rainfall by Dowdy et al. (2015).

Climate models, such as from the CMIP5 ensemble, generally simulate increased rainfall in the global mean under future global warming (e.g. Kharin et al., 2013), but for many locations there is a wide range of change with often both increases and decreases (Collins et al., 2013, Fig. 12.22). Narrowing this range, and the associated uncertainty in projections, is a major research challenge, and an underlying motivation for the present study. In order to better understand the simulated changes, various authors (e.g., Watterson, 1998, Seager et al., 2010, and others reviewed by Collins et al., 2013) have considered the atmospheric moisture budget and how rainfall change may be linked with that in the horizontal transport or flux of water vapour.

Moisture flux data have not been readily available from past CMIP experiments, and although fluxes can be usefully approximated by combining wind and humidity from standard output, Seager et al. (2010) show that there can be significant biases, compared to fluxes calculated from all model levels and time steps. In any case, multi-model analyses in the IPCC Assessment Reports have not focused on this transport, or indeed the vertically-integrated

atmospheric water vapour ('water vapour path', or 'precipitable water'), despite that being a standard output variable in CMIP5. Nevertheless, in recent years this and the vertically-integrated fluxes, which are key terms in a simplified, two-dimensional atmospheric moisture equation, along with precipitation, have been the focus of many studies of the tropical monsoons (e.g. Guo et al., 2018; Keane et al., 2019) and of atmospheric rivers (e.g., Chen et al., 2020), which both provide moisture for heavy rainfall. In some studies of atmospheric rivers, the magnitude of the flux vector is denoted IVT (for integrated vapour transport). Integrated fluxes are now available in the ECMWF's Reanalysis 5 (or ERA5) data set (Copernicus Climate Change Service, C3S, 2017).

A common approach of the above studies in understanding rainfall change is to consider the 'thermodynamic' influence of greater atmospheric water vapour under warming and the 'dynamic' influence of changes in the atmospheric circulation and associated weather patterns. From the moisture budget, much of the effect on changes in mean rainfall is driven by the convergence of flux. Held and Soden (2006) approximated the thermodynamic change in that using a scaling by temperature. We consider a related approach.

The data specification for CMIP6 (Eyring et al., 2016) includes vertically-integrated eastward and northward fluxes as output variables. At the WCRP/CMIP6 Workshop in March 2019, Watterson et al. (2019) presented analyses of data simulated by six models, which demonstrated spatial relationships between the flux and rainfall in both a 'base climate' representing the 'recent past' and a future change of climate under global warming. These climates were derived from the core experiment of CO_2 concentration increasing at 1% yr^{-1}, denoted 1pctCO2 (details provided shortly), which has previously been used in studies of the dependence of precipitation on temperature change (e.g., Li et al., 2013). While there are CMIP6 experiments with potentially more realistic forcing scenarios for the 21st century, the flux variables have not been requested for these, and little is currently available. In any case,

the 1pctCO2 experiment is well suited to generating the global field of standardized change, or change per degree of global warming, from a model. Where convenient, standardized change will be denoted by Δ. Under the pattern scaling approximation (Collins et al., 2013, section 12.4.2) the standardized change provides a useful representation of the pattern of change for various forcing scenarios. Furthermore, an ensemble of fields on a common grid can be readily used to explore relationships between variables. For example, Watterson (2019) correlated grid point values with indices of change in sea surface temperature (SST) across 40 CMIP5 models. Hope and Watterson (2018) used composites of data, from months with high monthly rainfall at spatial grid points, to examine the relationships between heavy rainfall and surface temperature. This approach can be applied to fluxes also.

To provide timely support for the IPCC's Sixth Assessment Report, this study extends the initial analyses by Watterson et al. (2019) using the available CMIP6 1pctCO2 moisture data. The vertical integral for flux and water vapour is assumed in the following, unless otherwise specified. The main aim is to assess how the convergence of the flux and the water vapour path relate to the rainfall, and to the range of change in rainfall across the ensemble. The following section briefly describes the methods used, starting with the equation for atmospheric moisture, then a partition of flux changes into (indicative) thermodynamic and dynamic components using only the change in water vapour path, and the analysis of high monthly rainfall. The data sets used are described in Section 3, including from a small ensemble of ten CMIP6 models. Seasonal climatologies for the base climate, from an initial 20-year period denoted P1, are presented in Section 4, including the high monthly rainfall. Standardized changes are presented in Section 5. Relationships between quantities are then analysed in Section 6, focusing on spatial correlations between ensemble averages, or multi-model means, and correlations across the models at points. The conclusions follow in Section 7. Supplementary material comprises Figures S1 to S10.

2. ANALYSIS OF ATMOSPHERIC MOISTURE

2.1 Vertically-integrated moisture equation

With the focus of the analysis being the supply of moisture for precipitation P from the atmosphere, the atmospheric moisture budget can be written (e.g., Watterson, 1998; Guo et al, 2018)

$$P = E + C - \partial W / \partial t \quad (1),$$

where E is evaporation from the surface, $C = -\nabla . \mathbf{F}$ is the convergence of the vertically-integrated horizontal moisture flux, vector **F**, and W is the integrated water (vapour, liquid and ice). Following Ye et al. (2019),

$$\mathbf{F} = g^{-1} \int_0^{p_s} q \, \mathbf{V}_h \, \mathrm{d}p \quad \text{and} \quad W = g^{-1} \int_0^{p_s} q \, \mathrm{d}p, \quad (2),$$

where g is gravity, p_s is the surface pressure, q is the specific humidity, and $\mathbf{V}_h$ is the horizontal wind vector. In models these calculations are discretised and adjustments may be required to conserve water, combining all its forms. The estimation of moisture flux has often involved extraction of daily (preferably more frequent) wind vector and moisture data from model levels (at least through the lower troposphere, where most of the humidity resides), and the calculation of the product and the integral. It is a great advantage to be able to use a provided data set of **F**, and ideally its convergence, as used within a model simulation. To calculate C, we use NCL's centred finite difference function uv2dv_cfd (with a one-sided difference at the polar latitudes), giving an approximation to the model calculation, albeit with some numerical noise.

The CMIP6 names for the quantities assessed here are tas for surface air temperature, pr for precipitation (P in Equation 1), prw for water vapour path (W) and intuaw, intvaw for the vertically integrated moisture transport (**F**). We use these names, except for calling the vector

'flux', and its convergence (C) 'conv'. We do not attempt to evaluate the complete water budget, but look for relationships between terms, based on the available quantities. With the liquid and ice components being typically 1% of the total moisture (see also Park et al., 2013), we use prw and flux without regard to whether those components are included. Conveniently, all these variables are two dimensional.

2.2 Partition of changes

In the context of a future globally warmer climate, and following Collins et al. (2013, p1077), changes in precipitation may be partitioned into a thermodynamic component, related mostly to water vapour changes, and a dynamic component, related to atmospheric circulation changes. For the horizontal moisture flux, these components have often been defined by changing either the winds or the humidity within the vertical integral (e.g. Seager et al. 2010; Keane et al. 2019). Watterson (1998) avoided the integral by using an approximation involving prw and an effective velocity. We propose an even simpler approach to determining an indicative thermodynamic change in a quantity: multiplying the fractional change in prw with the base climate or P1 value of the quantity. This is akin to the 'Clausius-Clapeyron scaling' used by Held and Soden (2006, Equation 6), where the factor is 7%, per degree of warming, which they applied to $P - E$, as a close approximation to the climatological convergence. As Seager et al. (2010) showed, much of their thermodynamic component followed from the increased saturation humidity. Assuming the fractional increase in humidity is near-constant in the lower troposphere, this fraction is similar to the fractional change of prw. Detailed assessments of the moisture budget by O'Gorman and Schneider (2009) and Chen et al. (2019) found that the change in prw is typically a little higher, because of greater warming in the upper troposphere. An indication of the sensitivity to this will be given. The difference of the net change and our thermodynamic component is assumed here to be the 'dynamic' component, although this would include nonlinear and other terms. (The

change in prw is wholly thermodynamic under this approach – Watterson (1998) applied an alternative one.)

Here we focus on the seasonal climatological conv from a model, and use its standardized change in prw, as a fraction of the P1 prw, in determining the thermodynamic component of the standardized change in conv. This is denoted as Δconv_T, with T for 'thermodynamic'. The remaining change is denoted Δconv_D, with D for 'dynamic'. Using the notation from Equation (1), these calculations can be expressed as

$$\Delta C_T = C_1 \frac{\Delta W}{W_1} \quad \text{and} \quad \Delta C_D = \Delta C - \Delta C_T, \tag{3}$$

where subscript 1 is for P1. As used only in selected plots, the flux can be partitioned similarly. (Note that the convergence of each component of the flux would only approximate the corresponding component of conv from Equation 3.)

2.3 Composites for high monthly rainfall

The analysis of extreme monthly precipitation previously applied to CMIP5 by Watterson et al. (2016) has been applied here to two 20-year periods (starting with P1) of data from each of our CMIP6 simulations. At each model grid point, the top decile of monthly rain rate values in each of the four seasons is determined in each period. The usual three-month seasons are used, with a focus on December–February or DJF and June–August, JJA. For each season and period there are 60 individual months so the top decile forms an 'H' composite of the six highest values. Hope and Watterson (2018) determined composites of anomalies of various quantities for the six H months, or times lagged before or after by up to several months, at each individual point. We focus on the composites of the actual values of pr, prw, conv and flux for the high-rainfall months (i.e. at lag 0) at each point. These composites are denoted here as, for example, pr-H. As for the other variables, the composite conv field is calculated by averaging the conv values from the individual months specified at each model grid point.

This is different to the convergence of the field of composite fluxes, which uses fluxes at adjacent points often from different months and is very noisy.

3. DATA SETS

3.1 CMIP6 simulations

The models whose 1pctCO2 simulations are analysed are listed in Table 1, along with their official institution, following the CMIP6 designations, and a three-character code name used here for convenience. Early submissions to the CMIP6 archive included CNRM-CM6-1 (code cn6) and CNRM-ESM2-1 (code cne) from CNRM-CERFACS and IPSL-CM6A-LR (i6e) from IPSL, both modelling centres being in France. These submissions included all the variables that are needed for our analyses, in the monthly-mean form. Note that most monthly atmospheric variables are included in the 'Amon' table of CMIP6, while the flux variables are listed under 'Emon', the 'extension' table. Models cn6 and cne have a relatively high horizontal resolution, with a representative grid length of 125 km, and high number of atmospheric levels, both given in Table 1. Model cne has additional components such as ocean biogeochemistry, making it an Earth System Model (ESM), as has i6e, and in the code this is designated by 'e' as the third character. Data from a version of cn6 with higher resolution, CNRM-CM6-1-HR (code cnh) is also available.

We had anticipated that with 1pctCO2 being a core experiment, other groups would often submit the flux for it, however this has not been common. The MOHC, from the UK, has submitted flux from their ESM model, UKESM1-0-LL (hue), and this includes atmospheric transport of ice and liquid water. The standard model, HadGEM-GC31-LL (h3l) at the same resolution, denoted N96 (with a grid of 144 latitudes and 192 longitudes), and a model with higher resolution, N216 (324 and 432), HadGEM3-GC31-MM (h3m) have also been submitted, but without full flux data. For both these models, we have therefore accessed the

data for the two periods directly from MOHC. The available flux data are for the transport of water vapour. This flux output is also available from the two models submitted by CSIRO, Australia: ACCESS-CM2 (ac2) and ACCESS-ESM1-5 (ace). These also use the MOHC's atmospheric Unified Model (UM), on an N96 grid, although the ESM model has an earlier version of the UM. The Australian models have ocean and land components that are different from the MOHC models, as is documented on the CMIP6 webpages. The MIROC team from Japan has submitted data from the low resolution MIROC-ES2L, code mce. All ten simulations are designated as the first (i.e., 'r1') from the model. Further details on the models are provided in the following references: cn6, Voldoire et al. (2019); cnh, Voldoire (2019); cne, Séférian et al. (2019); i6e, Hourdin et al. (2020); h3m and h3l, Williams et al. (2017); hue, Sellar et al. (2019); ac2, Bi et al. (2020); ace, Law et al. (2017) and Ziehn et al. (2020); and mce, Hajima et al. (2020).

While the formulations of these ten models are not as diverse as the full CMIP6, the multi-model mean of this small ensemble should provide climatological means that can represent the relationships between simulated quantities. To form this, the individual model fields are interpolated onto a common one-degree global grid, on which the average, denoted here av10, will be analysed. This is done for both the base climate and the standardized change fields, including the H composites and change components.

3.1.1 Global mean warming

The 1pctCO2 experiment starts from a nominal 1850 state, taken from a 'control' simulation of 'pre-industrial' climate. The atmospheric CO_2 concentration (prescribed to be spatially uniform) increases at 1% per year for 150 years. From each model the global mean tas rises steadily, at a rate that depends on the model, as illustrated in Figure S1. For the averaging periods used in the analyses, we retain the 20-year length used in previous studies. For the base climate, we use years 2-21 of the simulation, denoted P1, while the high-

warming period at the end of the experiment, or P2, is from years 131-150. To define 20 DJF seasons with consecutive months, the first season starts in the previous December. The P1 climate should approximate the climate of the recent past, before substantial warming, although the mean temperature is typically only a little higher than that of the initial state. (Note that the CMIP6 'historical' experiment should be used for realistic climates over the past century.)

The change in global mean tas, from P1 to P2, is given for each model in Table 1 and ranges from 4.3 °C to 6.5 °C. It is worth noting that the CO_2 concentration in the 1pctCO2 simulation rises by a factor of 3.6 from P1 to P2 (between central years). This and the warmings are around the top of the range of those projected from pre-industrial to the end of the 21st century, under a high emissions scenario (Collins et al. 2013, section 12.3.1.1, Figure 12.5).

The full series of seasonal and annual means used are of 149 yearly values. When possible, the standardized changes are defined, following Watterson (2019), using regression over all values with the annual global mean tas series. In the case of the high monthly rain analyses, or when the data set is limited, the difference P2 minus P1 is used, scaled by the corresponding change in tas. In forming standardized changes, maximizing the climate change signal by using periods at the ends of the simulations should reduce the statistical uncertainty from unforced interdecadal variability. Tests show that there is minimal difference between the results from the two methods, although statistical uncertainty is, in theory, smaller when all years are used.

3.2 ERA5 Reanalysis data

Atmospheric 'reanalyses' produced by weather models that assimilate global observations, including soundings of winds and humidities, can provide gridded integrated moisture fluxes in a comparable form to those of the CMIP6 models. The ECMWF product ERA5, using a

highly resolved modelling system than can be considered state-of-the-art and recently released in monthly-mean form, is considered here. While past reanalyses have had limitations in the moisture budget (e.g., Berrisford et al., 2011), Hersbach et al. (2020) find that ERA5 provides an improved global moisture budget and rainfall distribution. Since our data set starts with year 1979, we present climatological results from ERA5 only for qualitative comparison with those from CMIP6. The years averaged are 1980-2017, starting with the previous December. ERA5 includes the vertical integrals of eastward and northward water vapour flux, and also the 'divergence of moisture flux'. We use these, along with the integral of water vapour, the 'mean total precipitation rate', and surface air (at 2m) temperature. The ERA5 data grid spacing is 0.25°, but for the global plots the data are interpolated to a one-degree grid. We do not consider other observational moisture data sets here, but Rodell et al. (2015) and Robertson et al. (2016) provide a comparison of moisture budget terms from several data sets.

4. CLIMATOLOGIES FOR THE BASE CLIMATE

4.1 Mean quantities

The seasonal climatological fields for the P1 base climate from each model have been calculated and are presented as representing the recent past. The global and annual means of tas (Table 1) range from 12.6 °C to 15.1 °C, which is typical of the variation in simulated pre-industrial climates within CMIP experiments. The av10 value of 13.8 °C is actually only a little smaller than the ERA5 1980–2017 mean, 14.2 °C. While a closer match could be obtained by extending the P1 time span, the effect on the moisture fields would be limited. For the present purposes the P1 fields should be adequate.

To provide an example of fields from all individual models, we select a region with some of the most intense climatological fluxes, Southern Asia during the summer monsoon. Figure 1 shows the JJA climatology for pr and flux on the model grids. All ten models provide a

reasonable match to the patterns represented by the ERA5 data, shown in the top left. Flux impacts the west coasts of India and Indochina, where there is high mean rainfall. Northward flux extends to the Himalayas, where rainfall is also high. Rain is less intense in the lower resolution models i6e and mce, and more intense, and sharpest, in the high-resolution h3m and cnh. In some cases, the rainfall is more intense than in ERA5: for example, cn6 overestimates the high coastal rainfall, as also shown by Voldoire et al. (2019, their Figure 5, using observational data). A tendency for the UM to have a dry bias over India is evident in all five UM-based models, particularly for ac2, but less so for h3m. In any case, the av10 fields produce all the features seen in ERA5 in this domain. A plot of the differences, Figure S2, shows that the ensemble mean is, nevertheless, a little drier over much of India. Fluxes in the Bay of Bengal are not quite as strong as in ERA5, and rainfall over the Himalayas is less intense.

The similarity of av10 and ERA5 generally extends to the globe and each season, with both DJF and JJA shown in Figure 2. The fluxes are again shown, but pr is replaced by prw. High prw prevails in the low latitudes, in both models and reanalyses. There is often a peak in prw in monsoonal regions, such as India and the Caribbean in JJA, and Brazil and northern Australia in DJF. Plots of the differences, in Figure S3, reveal some inaccuracy in the position of the bands of high prw and adjacent fluxes. In both av10 and ERA5, the anticyclonic flow over subtropical oceans in summer is striking. Naturally, there is a large seasonal cycle in prw at high latitudes. There is a small cycle in pr and prw in the av10 global means also, with values for four seasons given in Table 2. Even locally, though, variation in prw provides only a very small contribution to the climatological budget (Equation 1), in contrast to evaporation (e.g., Park et al., 2013).

The seasonal convergence fields for av10 are shown in Figure 3, alongside pr, with flux vectors overlying both. The low-latitude peaks in prw tend to coincide with the peak

convergence and also rainfall. Peaks of rainfall and convergence coincide in many midlatitude places also, notably along western coasts of the Americas, Europe, Japan and New Zealand. It is worth noting that the annual means averaged over all land (land fraction 0.308) for pr/conv are 2.37/0.79 mm d^{-1}, which compares with 2.29/0.71 mm d^{-1} from ERA5 and observational estimates of 2.18/0.86 mm d^{-1} from Rodell et al. (2015). Of course, globally convergence is balanced by an equal amount of divergence (Table 2). Subtropical regions with high divergence (Figure 3) tend to have low rainfall, while low rainfall over desert regions is generally associated with near-zero conv, although the fluxes can be moderate. Most of these features in av10 are well matched to those in ERA5 (and the corresponding Figure S4). Differencing of fluxes can lead to a noisy conv field. At the poles, an erroneous result follows in models whose flux components are not accurately defined to represent a flow across the pole.

4.2 High monthly rainfall

For each model in turn, the top decile of monthly pr values at each point within the 20 3-month seasons of P1 were determined, and the average taken to form the H composite for each seasonal case. After interpolating each model field to the common grid, the av10 field was calculated. The resulting pr-H fields for DJF and JJA are plotted in Figure 4. The patterns are similar to the means in Fig. 3, with the ratio of H to the mean being typically 2 to 3. From values given in Table 2, the ratio of the global means is 2.1 for DJF and 2.0 for JJA. Averages of values from the same months at each point were calculated for the flux and conv fields, to complete Figure 4. The pattern for conv-H is similar to that for conv, but values are mostly more positive, with smaller regions of divergence. The global mean conv rises from 0.0 for the all-month case to H values 2.9 mm d^{-1} for DJF and 2.7 mm d^{-1} for JJA, nearly as much as the rise for pr, of 3.3 mm d^{-1} for DJF and 3.1 mm d^{-1} for JJA (see Table 2 for all seasons). The pattern for flux in H is also similar, often with somewhat larger magnitudes. While such

enhanced fluxes would indicate greater transport through the point with high rain, it is the convergence there that is important. These relationships are further quantified in Section 6. Note that the change in prw during high rainfall months, as well as evaporation, contribute to the moisture budget (Equation 1).

5. STANDARDIZED CHANGE

5.1 Mean quantities

The standardized change is the change per degree of global warming, based on the 1pctCO2 simulation from each model. For convenience, 'per degree of global warming' is usually omitted from the units given in various results, so they effectively represent change at one degree of annual and global mean warming. The actual changes for that warming may differ if the response is not linear, but it differs across models in any case. The mean across the 10-member ensemble of the field of standardized change in warming (Δtas) depends on the season, as can be seen in Figure S5. Values at high latitudes exceed 3 (°C) in winter, but in summer are more typical of land generally, 1 to 1.5. The multi-model mean standardized change for prw (also in Figure S5, along with moisture flux for each season) is largest in the tropics, as expected for this absolute (non-percentage) change, but also has a pattern with considerable dependence on the local surface warming, and both quantities universally increase. From values given in Table 2, the change in the global mean prw, per degree, as a percentage of the P1 climate value, is 7.6% in DJF and 7.9% in JJA. The fields for the av10 of percentage change are shown in Figure S6, with increases of typically 6 to 10%, but more where warming is much larger than average.

We focus on the rainfall and flux changes, and Figure 5 illustrates the individual models for the same summer monsoon case as Figure 1. For each the pattern of flux change in this region resembles that for the base climate (noting the much smaller reference vector scale)

broadly indicating an intensification of fluxes with increasing temperature. Similarly, in most models, the rainfall increases in the high rainfall regions of Figure 1, including the west coasts and Himalayas. The av10 patterns are similar in Figures 1 and 5, although there are some regions of high P1 rainfall with a decline, e.g. the west coast of India at 12°N, and the Annamite Range of eastern Indochina. The av10 convergence result, in the top-left of Figure 5 provides a very close match to av10 Δpr. Evidently, relatively subtle changes in the flux relate to spatial variations in rainfall change and to differences between models. For instance, rainfall increases in far southern Vietnam in models with strengthened flux from the south, but not in cn6 and cne, with no change in mean flux. The plot of the av10 Δpr minus Δconv, shown in Figure S7, indicates some differences that indicate changed evaporation, including a small increase over some seas.

The global fields for av10 changes in two seasons are shown in Figure 6. The pattern for flux again reflects an enhancement of the base climate, under warming. The global mean magnitude of the standardized flux vector is around 7% of the P1 value, which is close to the prw result. Along much of the equatorial zone there is a large increase, in mm d^{-1} terms, for both pr and conv. The areas of strong convergence in P1 (Figure 3) often have increases, while strong divergence tends to become stronger. Although there are many areas of high rainfall with increases, some bands of change in pr do not coincide with bands in P1. For example, in av10 the central equatorial Pacific has a low pr band in DJF, but a strong increase, while northern South America is wet in JJA and has a decrease. The pr and conv change fields resemble each other, and the same contours can be used (in contrast to Figure 3), given that the mean of the Δpr field (Table 2) is now small relative to the spatial variation. Nevertheless, the widespread increase in pr at high latitudes in winter is not well matched by Δconv (which has decreases in the Arctic Ocean –presumably, E increases). The customary multi-model result, of change in pr as a percentage of the base climate of each model, is

shown in Figure S8. Comparable values for the increases to those in prw (Figure S6), and some similarity in patterns, reflect the importance of atmospheric moisture to rainfall amount.

5.2 Thermodynamic/Dynamic partition

Changes resulting from an enhancement of humidity under warming are consistent with a thermodynamic change. Using the simple approach proposed in Section 2.2, an indicative thermodynamic change in a field was derived by simply multiplying the base climate seasonal field by the local fractional change in prw, for each model. The resulting multi-model means for conv and flux, along with the 'dynamic' residual are shown in Figure 7. Certainly, for the Southern Asia summer monsoon, this thermodynamic component in Δconv, from a local prw increase of around 8% (per degree, Fig. S6), provides much of the pattern in the total. Even there, the dynamic component leads to little net change in rain over much of India. In various other monsoonal regions with convergence of flux in the base climate, the thermodynamic term again provides water for the increased rain, especially over the land. Often, the dynamic term removes water, with net decreases over the ocean. In the dry subtropics, the opposite signs tend to prevail, with the thermodynamic term amplifying divergence of flux in the base climate. The dynamic term partly offsets this, but from Equation (1), changed evaporation from the ocean surface can also contribute, and lead to little change in pr. At higher latitudes pr generally increases, largely driven by the thermodynamic influence. These results are broadly consistent with the assessment of monsoon regions by Endo and Kitoh (2014), and elsewhere by the other studies cited. Note that the global mean of each Δconv component is near-zero in each season (around 0.01 mm d^{-1} for $\Delta conv_T$ and –0.01 mm d^{-1} for $\Delta conv_D$). The global standard deviation, as a measure of magnitude, is some 10% larger for $\Delta conv_D$.

As a test of the sensitivity of this partition to using prw to determine the thermodynamic scaling, changes in specific humidity have been evaluated from pressure level data from one model (cn6). The standardized change of the global mean at 850 hPa (or the level above the

surface, if needed) was 6.8%, compared to 8% for prw, a ratio of 0.85. Figure S9 shows the result of applying a (smaller) factor 0.75 to the thermodynamic fields of Figure 7. Naturally, the Δconv_D term becomes relatively larger, but qualitatively, the partition is very similar.

5.3 High monthly rainfall

The standardized change in the top decile of monthly rainfall for each seasonal case is calculated from the composites in the two time periods, P1 and P2, determined at each grid point. The P2 minus P1 values are divided by the change in tas (annual, from Table 1). The av10 fields for Δpr-H in two seasons are shown in Figure 8. The pattern of change is similar to that for (all-month) mean pr, but values tend to be more positive and increases in monsoon regions are much more prominent. Even as a percentage, the global mean (Table 2) pr-H increases are nearly double those for mean pr, with the average over four seasons being 2.6% for H and 1.5% for mean. This is consistent with the generally larger percentage changes for rainfall extremes in CMIP5 (e.g., Kharin et al., 2013), including those for the top decile monthly amounts presented by Watterson (2020). Again, the pattern of change for conv-H is similar, and the global mean of this increases, by around 58% of the pr-H change, in mm d^{-1} terms (Table 2). Clearly, other budget terms contribute to the pr-H changes. The composite moisture fluxes (Figure 8) also tend to have a similar pattern to the all-month results (Figure 6), often with modest increases in magnitude. We do not attempt to partition Δconv-H, but note that several of the studies referenced have assessed changes in extreme daily rainfall.

6. RELATIONSHIPS BETWEEN RAINFALL AND MOISTURE VARIABLES

6.1 Spatial correlations

A broad theme in the description of the fields of pr, prw and conv, for all the variants presented, is the similarity in spatial patterns. It is worthwhile quantifying this using the spatial correlation coefficient, *r*, over the globe. Values for various pairs of av10 quantities for

each season are given in Table 3. Starting with the base climate (recent past or P1) fields, the similarity of pr and conv is moderate, with *r* values around 0.7, limited by the importance of evaporation in the moisture budget, Equation (1). Correlations for pr and prw are also moderate, with both being broadly larger at warmer latitudes. The high *r* between the mean (pr) and high monthly (pr-H) rain fields reflects a similar local ratio between the two statistics for most regions (Watterson et al., 2016). The link between pr and conv is enhanced with the H composite. This follows from the increased importance of conv, relative to other terms in the budget, as evidenced by the global means (Table 2), with conv-H being strongly positive. There is rather little difference in *r* between the seasons in all the results.

The comparison of P1 fields and change fields give contrasting results. For prw there is high correlation, with the (absolute) change being a relatively similar percentage of P1 (Figure S6) for most of the globe. For rainfall, there is little correlation globally, even for these ensemble means, corroborating the complexity of projecting future rainfall! Similarly, Chadwick et al. (2013) noted a correlation of only 0.2 over the tropics for annual fields from CMIP5. Our global results for conv (Table 3) are a little higher, but still rather weak. Restricting the domain and season to that of Figures 1 and 5, *r* is 0.25 for pr and 0.35 for conv.

Turning to pairs of change fields, for changes in pr and prw the correlations are larger when they are in percentage terms (Table 3), as the common high-latitude increases have greater weight. Changes in pr and conv (Figure 6) have higher correlations than the P1 fields. While the Δconv_T component is important to Δconv, for instance over the Southern Asia domain in JJA (with $r = 0.39$), its overall correlation with Δconv is similar to that between Δconv and conv P1. The Δconv_D term is moderately correlated with Δconv. In fact, the two components of Δconv are anticorrelated. The changes in H have a similar pattern to those for means, for both pr and conv. The similarity between pr and conv is highest of all for the

change in H composites (Figure 8), with $r \geq 0.95$. These results indicate an important role for both prw and conv in determining the spatial variation in the ensemble mean field of pr, and especially in the standardized changes of pr.

6.2 Correlations across models

Relationships between moisture quantities can also be sought from the range of values across the individual members of the ensemble, using fields on the common one-degree grid. We focus on pairs of standardized change quantities, for which there is a value of *r* across the ten models at each grid point. Of particular interest is the variation across the ensemble in the standardized rainfall change, since this must be reflected in the range of projected change, and hence its uncertainty. (Under pattern scaling, additional uncertainty follows from that in global warming.) The fields of *r* between percentage changes in pr and prw (Δpr % – Δprw %, for short) are shown for two seasons in Figure 9. Here, a high correlation at a grid point, such as over the Amazon in each case, indicates that a model with large Δpr % would also have a large Δprw %. There is considerable spatial variation in the *r* fields, and even some negative values, including over the Arctic Ocean in summer. This variation is likely enhanced by statistical uncertainty, given the small ensemble (of ten). However, Watterson (2020) showed that for changes in 23 CMIP5 models, the correlation also has much spatial variation, with peaks exceeding 0.8, as in Figure 9.

While a larger ensemble is needed for reliable regional values, the global mean of a correlation field should be indicative of the overall strength of a relationship. Global means of the fields from Figure 9, and for five other pairs of change variables, are given in Table 4. For Δpr % – Δprw %, the means are around 0.45 –positive, but only moderate. The means are only a little less for changes in absolute terms (which can be affected by the differences in base climates). Evidently some of the range in Δpr can be related to that in Δprw, especially over oceans. The supply of the moisture is associated with conv, and as for spatial variation

(Table 3), the mean correlation for Δpr – Δconv in each season is higher than for Δpr – Δprw. As for the spatial case in Table 3, the dynamic component is moderately correlated with Δpr, while Δpr – Δconv$_T$ has near-zero mean *r* in each season. The most consistently high value is between change in pr-H and change in conv-H. For much of the tropics, and also many land points in higher latitudes, *r* is well over 0.8 (Figure S10).

6.3 Some implications for projections

Given the relationships between pr, prw and the moisture flux convergence, in the present climate, the links in change fields, both spatially and among ensemble members, are not surprising. An opportunity provided by the CMIP6 flux fields would be to extend the evaluation of present climate simulations to these related quantities. Model projections of changes in those related quantities that are correlated with changes in rainfall would provide further information about the possible range of future rainfall changes. This would particularly be the case for regions where the correlations are particularly large (as shown, for example, in Figs. 9 and S10). It is revealing to see the strengthening relationship between pr and conv, for the standardized changes assessed here, and for the composites of heavy monthly rain. The underlying causes of the range in regional change between models have not been addressed here. Numerous studies (including the projections of CSIRO and Bureau of Meteorology, 2015, and Chadwick et al. 2017) have linked changes in mean rainfall to mode-like changes in the mean circulation, especially when these are associated with changes in SST (such as El Niño-Southern Oscillation). Watterson (2020) demonstrated that, in the CMIP5 ensemble, such links can be extended to heavy rainfall in Australia and parts of Asia. If the vertically-integrated moisture flux and water vapour path outputs can be obtained from more CMIP6 models, further insights should be obtained. Potentially, models with realism in the present climate simulations of the moisture budget components may provide more consistent future changes in both mean and heavy rainfall.

7. SUMMARY AND CONCLUSIONS

The wide range of projections of regional rainfall based on the CMIP5 ensemble provides a motivation for further studies of the atmospheric moisture budget using CMIP6. We take advantage of the new CMIP6 variables, the vertically-integrated eastward and northward moisture transport (intuaw, intvaw) or flux, and provide a multi-model assessment of these, their convergence, along with water vapour path, prw. Fluxes were obtained from the 1pctCO2 simulations of ten models, in which the global warming between a 20-y base climate and the final 20-years ranged from 4.3 °C to 6.5 °C. Seasonal climatologies of the base period for pr, prw, flux and its convergence were presented. As a regional example, the Southern Asia summer monsoon was represented in each model, with higher intensities reached in HadGEM3-GC31-MM and CNRM-CM6-1-HR, the models with smaller grid lengths. While evaluation of the CMIP6 present climate should be conducted with more realistic scenarios, the mean base climate resembled well climatological fields from the ERA5 reanalysis. Composites 'H' of quantities for months in the top decile of monthly rainfall, calculated at each model grid point, produced a field of heavy rainfall, around double that of the mean. Spatial correlations between the seasonal fields were typically 0.7 for pr and conv, rising to 0.9 for the H fields.

Fields of standardized change (Δ), or change per degree of global warming, were calculated from the full time series, or from the base and last 20-y periods (in the H case). In the multi-model mean, there is a strong increase (in mm d^{-1} terms) in rainfall and convergence along much of the equatorial band, including for H composites, in each season. Water vapour path increases everywhere, typically by 6 to 10 % per degree of warming. The ensemble-mean Δpr is only weakly correlated (0.2) with the base climate pr, and that for conv little better (0.3). However, Δprw is highly correlated with the base prw, pointing to the importance of the 'thermodynamic' change in that variable. A simple definition of that change in other variables

used the fractional change in prw as a product, with the residual being 'dynamic' change. The component Δconv_T is important to Δpr in the Southern Asia monsoon region, where flux tends to strengthen, but globally Δconv_D is more strongly correlated. The net Δconv is highly correlated with Δpr, around 0.9. This rises to 0.95 for the heavy-rain composites, for which Δconv-H provides a close match to Δpr-H over most the globe. These results suggest that when weighting model projections of future rainfall change, it may help to see how well they simulate quantities other than pr in the current climate, particularly when looking at extreme rainfall, where the correlations are higher.

Relationships between changes in pr and other components hold at grid points also, when the individual model results are correlated. The global mean of the correlation fields rises from around 0.40 for the pair Δpr – Δprw, to 0.6 for Δpr – Δconv, and 0.7 for Δpr-H – Δconv-H, with larger values in some regions. Clearly, there is a dependence in the change in pr with that in conv, particularly for heavy rainfall. The range in rainfall change is linked to that in the fluxes, which may provide insight into the associated moisture sources. Assessment of a larger ensemble from CMIP6, using the new flux variables, has the potential to aid in the evaluation of these processes, and potentially allow more confident projections in future rainfall changes.

Acknowledgements: We acknowledge the World Climate Research Programme, which, through its Working Group on Coupled Modelling, coordinated and promoted CMIP6. We thank the climate modeling groups for producing and making available their model output, the Earth System Grid Federation (ESGF) for archiving the data and providing access (at https://pcmdi.llnl.gov/CMIP6), and the multiple funding agencies who support CMIP6 and ESGF. We particularly acknowledge colleagues who contributed to the development of the UM-based models and the simulations used here, and who provided comments on the draft manuscript. The ERA5 data are downloadable, after registration, from

https://cds.climate.copernicus.eu. Calculations and plotting have largely been performed using the NCL software (NCAR Command Language, NCAR, Boulder, Colorado). TA was supported by the Joint UK BEIS/Defra Met Office Hadley Centre Programme (GA01101).

……..

REFERENCES

Bi, D. and coauthors (2020) Configuration and spin-up of ACCESS-CM2, the new generation Australian Community Climate and Earth System Simulator Coupled Model. *Journal Southern Hemisphere Earth System Science.* In press

Berrisford, P., Kållberg, P., Kobayashi, S., Dee, D., Uppala, S., Simmons, A. J., Poli, P. and Sato, H. (2011) Atmospheric conservation properties in ERA-Interim. *Quarterly Journal of the Royal Meteorological Society*, 137, 1381–1399. doi:10.1002/qj.864.

Chadwick, R., Boutle, I. and Martin, G. (2013) Spatial patterns of precipitation change in CMIP5: Why the rich do not get richer in the tropics. *Journal of Climate*, 26, 3803–3822. doi:10.1175/JCLI-D-12-00543.1.

Chadwick, R., Douville, H. and Skinner, C. B. (2017) Timeslice experiments for understanding regional climate projections: applications to the tropical hydrological cycle and European winter circulation. *Climate Dynamics*, 49, 3011–3029. doi:10.1007/s00382-016-3488-6.

Chen, G., Norris, J., Neelin, J. D., Lu, J., Leung, L. R. and Sakaguchi, K. (2019) Thermodynamic and dynamic mechanisms for hydrological cycle intensification over the full probability distribution of precipitation events. *Journal of the Atmospheric Sciences*, 76, 497-516. doi: 10.1175/JAS-D-18-0067.1.

Chen, J., Zhang, H., Ye, C., Chen, H. and Mo, R. (2020) Comparing atmospheric rivers over China and Australia: Two case studies. *Journal of Southern Hemisphere Earth System Science. in press.*

Collins, M., Knutti, R., Arblaster, J., Dufresne, J. L., Fichefet, T., Friedlingstein, P., Gao, X., Gutowski, W. J., Johns, T., Krinner, G., Shongwe, M., Tebaldi, C., Weaver, A. J. and Wehner, M. (2013) Long-term climate change: projections, commitments and irreversibility. Climate Change 2013. The Physical Science Basis, TF Stocker, D Qin, GK Plattner, M Tignor, SK Allen, J Boschund, A Nauels, Y Xia, V Bex, PM Midgley, eds., Cambridge University Press, 1029–1136.

CSIRO and Bureau of Meteorology (2015) 'Climate Change in Australia Information for Australia's Natural Resource Management Regions: Technical Report', CSIRO and Bureau of Meteorology, Australia.

Copernicus Climate Change Service (C3S) (2017): ERA5: Fifth generation of ECMWF atmospheric reanalyses of the global climate . Copernicus Climate Change Service Climate Data Store (CDS), (date of access June 2019) https://cds.climate.copernicus.eu/cdsapp#!/home.

Dowdy, A. J., Grose, M. R., Timbal, B., Moise, A., Ekström, M., Bhend, J. and Wilson, L. (2015) Rainfall in Australia's eastern seaboard: a review of confidence in projections based on observations and physical processes. *Australian Meteorological and Oceanographic Journal*, 65, 107-126.

Endo, H. and Kitoh, A. (2014) Thermodynamic and dynamic effects on regional monsoon rainfall changes in a warmer climate. *Geophysical Research Letters*, 41, 1704–1710. doi:10.1002/2013GL059158.

Eyring, V., Bony, S., Meehl, G. A., Senior, C. A., Stevens, B., Stouffer, R. J. and Taylor, K. E. (2016) Overview of the Coupled Model Intercomparison Project Phase 6 (CMIP6) experimental design and organization. *Geoscientific Model Development*, 9, 1937–1958.

Guo, L., Klingaman, N. P., Demory, M.-E., Vidale, P. L., Turner, A. G. and Stephan C. C. (2018) The contributions of local and remote atmospheric moisture fluxes to East Asian precipitation and its variability. *Climate Dynamics*, 51, 4139–4156. doi:10.1007/s00382-017-4064-4.

Hajima, T. and coauthors (2020) Development of the MIROC-ES2L Earth system model and the evaluation of biogeochemical processes and feedbacks. *Geoscientific Model Development*, 13, 2197-2244. doi:10.5194/gmd-13-2197-2020.

Held, I. M. and Soden, B. J. (2006) Robust Responses of the Hydrological Cycle to Global Warming. *Journal of Climate*, 19, 5686-5699.

Hersbach, H. and coauthors (2020) The ERA5 global reanalysis. *Quarterly Journal of the Royal Meteorological Society*. doi:10.1002/qj3803.

Hope, P. K. and Watterson, I. G. (2018) Persistence of cool conditions after heavy rain in Australia. *Journal of Southern Hemisphere Earth System Science*, 68, 41-64.

Hourdin, F. and coauthors (2020) LMDZ6A: the atmospheric component of the IPSL climate model with improved and better tuned physics. *Journal of Advances in Modeling Earth Systems,* in press. doi.org/10.1029/2019MS001892.

Law, R. M. and coauthors (2017) The carbon cycle in the Australian Community Climate and Earth System Simulator (ACCESS-ESM1) – Part 1: Model description and pre-industrial simulation. *Geoscientific Model Development*, 10, 2567–2590, 2017. doi:10.5194/gmd-10-2567-2017.

Li, G., Harrison, S. P., Bartlein, P. J., Izumi, K. and Prentice I. C. (2013) Precipitation scaling with temperature in warm and cold climates: An analysis of CMIP5 simulations. *Geophysical Research Letters*, 40, 4018–4024, doi:10.1002/grl.50730.

Keane, R. J., Williams, K. D., Stirling, A. J., Martin G. M, Birch, C. E. and Parker, D. J. (2019) Fast biases in monsoon rainfall over southern and central India in the Met Office Unified Model. *Journal of Climate*, 32, 6385-6402.

Kharin, V. V., Zwiers, F. W., Zhang, X. and Wehner, M. (2013) Changes in temperature and precipitation extremes in the CMIP5 ensemble. *Climatic Change* 119, 345–357. doi:10.1007/s10584-013-0705-8.

Murphy, J. M., Harris, G. R., Sexton, D.M.H., Kendon, E. J., Bett, P. E., Brown, S. J., Clark, R. T., Eagle, K., Fosser, G., Fung, F., Lowe, J. A., McDonald, R. E., McInnes, R. N., McSweeney, C. F., Mitchell, J.F.B., Rostron, J., Thornton, H. E., Tucker, S. and Yamazaki, K. (2018) UKCP18 Land Projections: Science Report. Met Office Hadley Centre, Exeter, UK.

O'Gorman, P. A. and Schneider, T. (2009) The physical basis for increases in precipitation extremes in simulations of 21st-century climate change. *Proceedings of the National Academy of Sciences USA*, 106, 14,773-14,777.

Park, H.-J., Shin, D.-B. and Yoo J.-M. (2013) Atmospheric water balance over oceanic regions as estimated from satellite, merged, and reanalysis data. *Journal of Geophysical Research,* 118, 3495–3505. doi:10.1002/jgrd.50414.

Rashid, H.A. and Hirst, A.C. (2017) Mechanisms of improved rainfall simulation over the Maritime Continent due to increased horizontal resolution in an AGCM. *Climate Dynamics*, 49, 1747-1764.

Robertson, F. R., Bosilovich, M. G. and Roberts, J. B. (2016) Reconciling land-ocean moisture transport variability in reanalyses with P - ET in observationally driven land surface models. *Journal of Climate*. 29, 8625–8646.

Rodell, M. and coauthors (2015) The Observed State of the Water Cycle in the Early Twenty-First Century. *Journal of Climate*, 28, 8289-8318.

Seager, R., Naik, N. and Vecchi, G. A. (2010) Thermodynamic and dynamic mechanisms for large-scale changes in the hydrological cycle in response to global warming. *Journal of Climate*, 23, 4651–4668.

Séférian, R. and coauthors (2019) Evaluation of CNRM Earth-System model, CNRM-ESM2-1: role of Earth system processes in present-day and future climate. *Journal of Advances in Modeling Earth Systems*, 11, 4182-4227. doi:10.1029/2019MS001791.

Sellar, A. A. and coauthors (2019). UKESM1: Description and evaluation of the U.K. Earth System Model. *Journal of Advances in Modeling Earth Systems*, 11, 4513-4458. doi:10.1029/2019MS001739

Voldoire, A. and coauthors (2019). Evaluation of CMIP6 DECK experiments with CNRM-CM6-1, *Journal of Advances in Modeling Earth Systems*, 11, 2177-2213. doi:10.1029/2019MS001683.

Voldoire, A. (2019) CNRM-CERFACS CNRM-CM6-1-HR model output prepared for CMIP6 HighResMIP. Version 20191021. Earth System Grid Federation. doi.org/10.22033/ESGF/CMIP6.1387

Watterson, I.G. (1998) An analysis of the global water cycle of present and doubled CO_2 climates simulated by the CSIRO general circulation model. *Journal of Geophysical Research*, 103, 23113-23129.

Watterson, I.G., Chua, Z.-W. and Hope, P.K. (2016) Extreme monthly rainfall over Australia in a changing climate. *Journal of Southern Hemisphere Earth System Science.*, 66, 402-423.

Watterson, I.G. (2019) Indices of climate change based on patterns from CMIP5 models, and the range of projections. *Climate Dynamics.* 52, 2451-2466. doi.org/10.1007/s00382-018-4260-x.

Watterson, I.G. (2020) Influence of sea surface temperature on simulated future change in extreme rainfall in the Asia-Pacific. *Asia-Pacific Journal of Atmospheric Sciences*, 56, 349-366. doi 10.1007/s13143-019-00141-w.

Watterson, I., Rashid, H. and Keane, R. (2019) Analysis of CMIP6 atmospheric moisture fluxes and the implications for projections of future change in regional rainfall. CMIP6 Model Analysis Workshop, 25–28 March. Barcelona, Spain.

Williams, K.D. and coauthors (2017) The Met Office Global Coupled model 3.0 and 3.1 (GC3.0 & GC3.1) configurations. *Journal of Advances in Modeling Earth Systems*, 10, 375-380, doi:10.1002/2017MS001115.

Ye, C., Zhang, H., Moise, A. and Mo, R. (2019) Atmospheric Rivers in the Australia-Asian Region: A BoM-CMA Collaborative Study, *Journal of Southern Hemisphere Earth System Science.* in press.

Ziehn, T., Chamberlain, M. A., Law, R., Lenton, A., Bodman, R. W., Dix, M., Stevens, L., Wang, Y.-P. and Srbinovsky, J. (2020) The Australian Earth System Model: ACCESS-ESM1.5. *Journal of Southern Hemisphere Earth System Science.* in press.

TABLE 1 Models used in the analysis. For each are given: the institution, a code name, representative grid length L in km, number of atmospheric levels, and simulated global and annual mean temperatures. The temperatures are for the base climate, period P1 (see Section 3.1), in degree Celsius, and the change to period P2. L is the side length of a square with the average area of the data grid squares over the globe. Models with code ending in 'e' have Earth System components. The code names are often modifications of names previously used for CMIP5 models by Watterson (2019). (* NERC, NIMS-KMA, NIWA).

Model	Institution	Code	L (km)	At. Lv.	P1 (°C)	P2 - P1
CNRM-CM6-1	CNRM-CERFACS	cn6	125	91	13.18	5.48
CNRM-CM6-1-HR	CNRM-CERFACS	cnh	44	91	12.64	5.71
CNRM-ESM2-1	CNRM-CERFACS	cne	125	91	13.92	5.02
IPSL-CM6A-LR	IPSL	i6e	157	79	13.07	5.53
HadGEM3-GC31-MM	MOHC	h3m	60	85	14.15	6.19
HadGEM3-GC31-LL	MOHC-NERC	h3l	136	85	13.88	6.49
UKESM1-0-LL	MOHC-*	hue	136	85	13.78	6.19
ACCESS-CM2	CSIRO-ARCCSS	ac2	136	85	14.06	5.54
ACCESS-ESM1-5	CSIRO	ace	135	38	14.68	4.28
MIROC-ES2L	MIROC	mce	250	40	15.11	3.61

TABLE 2 Global mean of ensemble mean (av10) quantities for both the base climate (P1) and the standardized change (Δ) for four seasons. Composites for top decile monthly rainfall are denoted by H. The unit is mm d^{-1}, except for mm for prw. The seasons are DJF (December–February), MAM (March–May), JJA (June–August) and SON (September–November)

Base climate	DJF	MAM	JJA	SON
prw	22.3	23.2	24.8	23.1
pr	3.05	3.06	3.14	3.04
pr-H	6.34	6.46	6.25	6.30
conv	0.0	0.0	0.0	0.0
conv-H	2.89	2.92	2.66	2.79
Change per °C	DJF	MAM	JJA	SON
Δprw	1.69	1.75	1.96	1.86
Δpr	0.05	0.05	0.04	0.05
Δpr-H	0.18	0.15	0.15	0.16
Δconv	0.0	0.0	0.0	0.0
Δconv-H	0.11	0.08	0.09	0.10

TABLE 3 Spatial correlation coefficient between quantities, using the av10 global fields, for each season. Results are in three categories: for two base (P1) climate fields, between base and change fields, and for two change fields. The standardized changes are in absolute terms, except for percentage changes denoted by %. Composites for top decile monthly rainfall are denoted by H. Thermodynamic/dynamic component is denoted by T/D.

Variable 1	Variable 2	DJF	MAM	JJA	SON
Base climate					
pr	conv	0.67	0.65	0.75	0.70
pr	prw	0.64	0.65	0.59	0.65
pr	pr-H	0.94	0.94	0.96	0.95
pr-H	conv-H	0.89	0.89	0.90	0.91
Base to change					
prw	Δprw	0.93	0.93	0.90	0.89
pr	Δpr	0.08	0.21	0.17	0.14
conv	Δconv	0.32	0.43	0.32	0.28
Change					
Δpr %	Δprw %	0.76	0.75	0.57	0.69
Δpr	Δprw	0.26	0.32	0.29	0.29
Δpr	Δconv	0.89	0.91	0.89	0.89
Δpr	$\Delta conv_T$	0.19	0.33	0.21	0.20
Δpr	$\Delta conv_D$	0.50	0.56	0.53	0.50
Δconv	$\Delta conv_T$	0.29	0.43	0.30	0.26
Δconv	$\Delta conv_D$	0.50	0.56	0.54	0.53
$\Delta conv_T$	$\Delta conv_D$	–0.68	–0.51	–0.64	–0.68
Δpr	Δpr-H	0.85	0.90	0.89	0.87
Δconv	Δconv-H	0.84	0.87	0.87	0.85
Δpr-H	Δconv-H	0.96	0.96	0.95	0.95

TABLE 4 Global mean of the correlation coefficient field for pairs of standardized change quantities, calculated from the ten model values at each point of the common one-degree grid. Composites for top decile monthly rainfall are denoted by H. Percentage changes are denoted by %. Thermodynamic/dynamic component is denoted by T/D.

Variable 1	Variable 2	DJF	MAM	JJA	SON
Δpr %	Δprw %	0.44	0.47	0.43	0.45
Δpr	Δprw	0.43	0.40	0.37	0.38
Δpr	Δconv	0.61	0.59	0.55	0.55
Δpr	$\Delta conv_T$	–0.01	–0.04	–0.06	–0.05
Δpr	$\Delta conv_D$	0.52	0.51	0.50	0.49
Δpr-H	Δconv-H	0.72	0.71	0.68	0.68

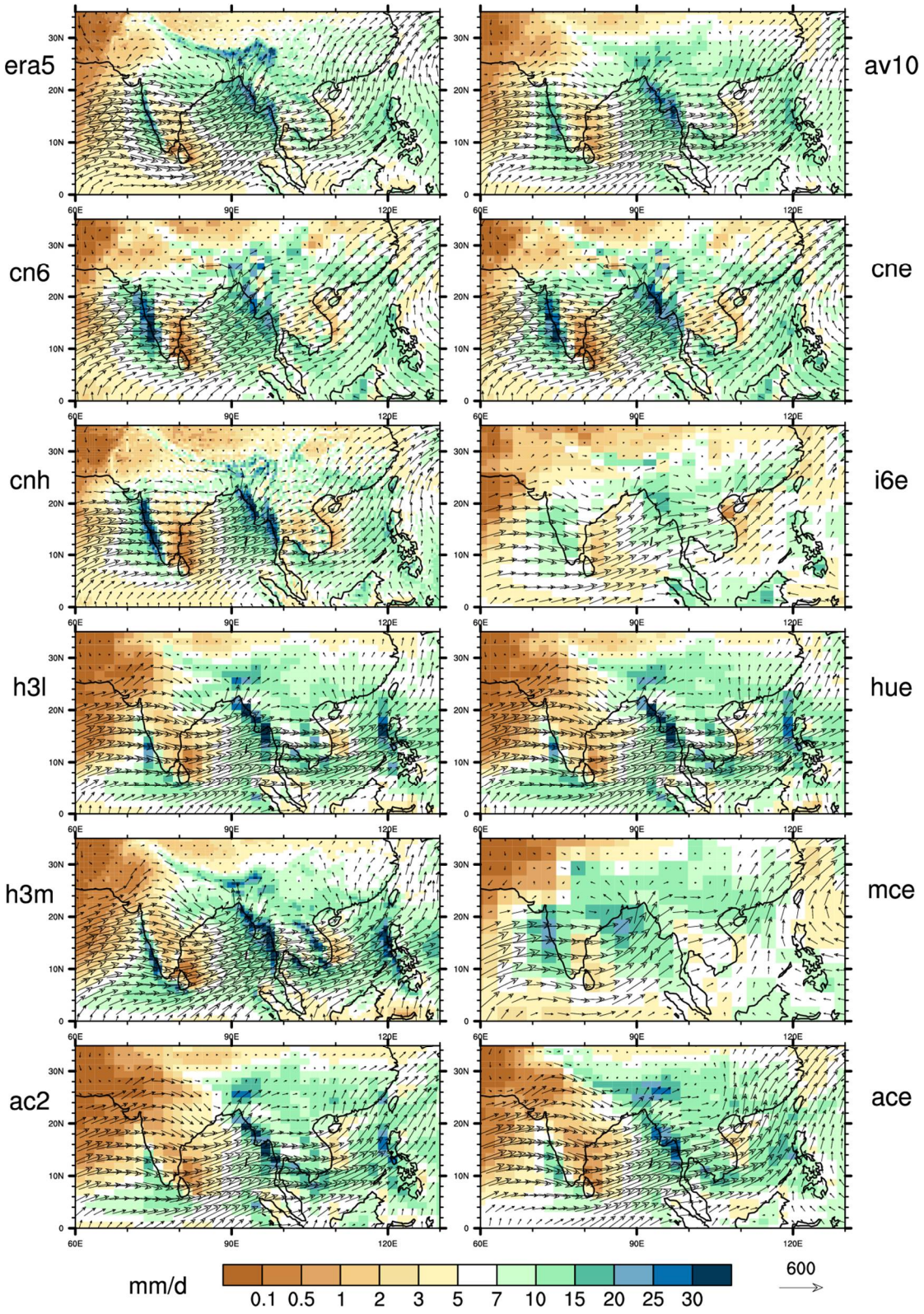

FIGURE 1 Climatological means from both ERA5 and ten models for the Southern Asia summer monsoon. The plots show the base climate JJA fields for precipitation, in mm d^{-1}, with moisture flux as a vector, with the reference vector being 600 kg m^{-1} s^{-1}. The top row shows ERA5 (1980–2017) and the av10 fields, with the others being the ten models, labelled by the code name. Vectors are shown at a spacing of not less than 0.3 of the reference vector length. The length and head size are proportional to the vector magnitude.

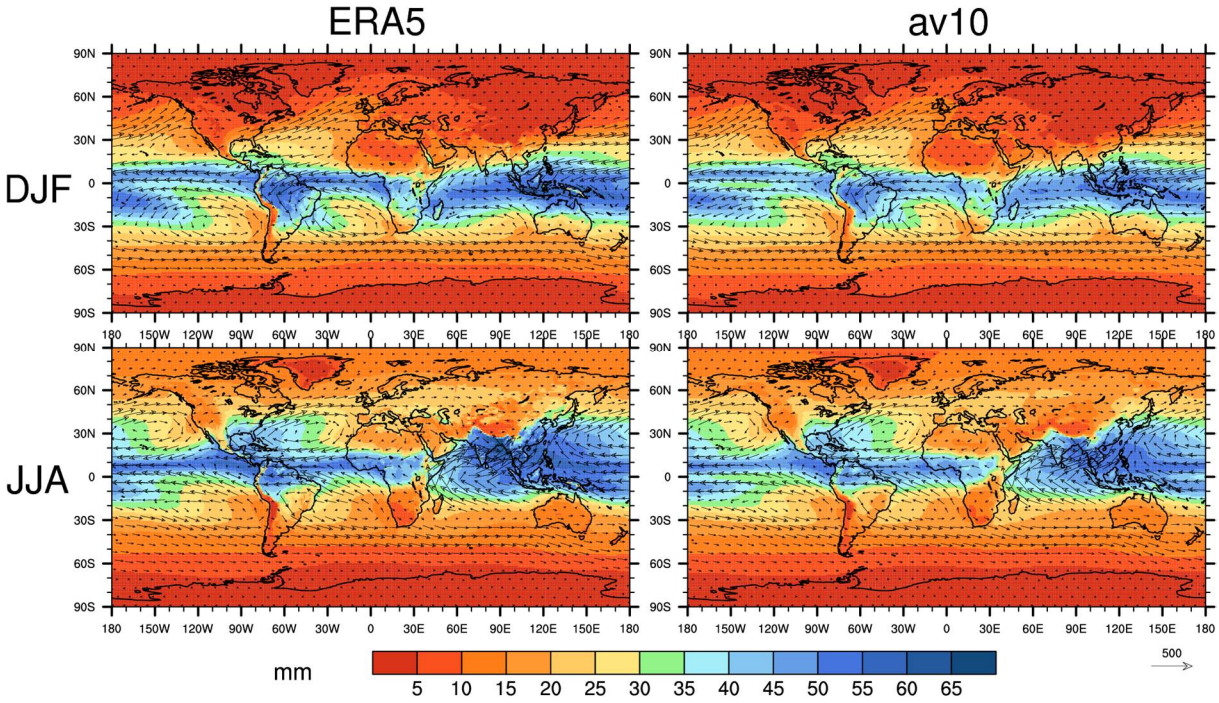

FIGURE 2 Climatological means from ERA5 (left) and av10 (right) in two seasons, top DJF, bottom JJA: for water vapour path (prw) in mm and moisture flux, with the reference vector being 500 kg m^{-1} s^{-1}. Vectors are shown at a spacing of not less than a quarter the reference vector length (likewise for other figures, unless stated).

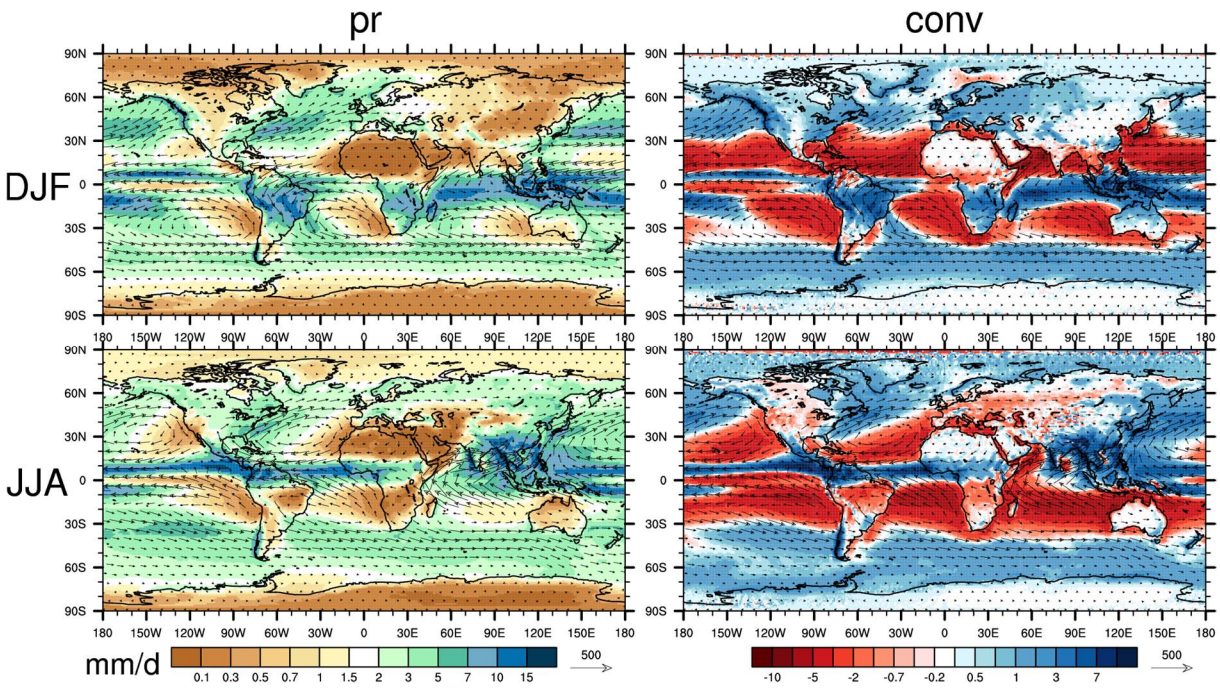

FIGURE 3 Climatological means from av10, in two seasons, top DJF, bottom JJA: precipitation (pr, left) and moisture convergence (conv, right), in mm d^{-1}. In both the vectors are the moisture flux, with the reference vector being 500 kg m^{-1} s^{-1}.

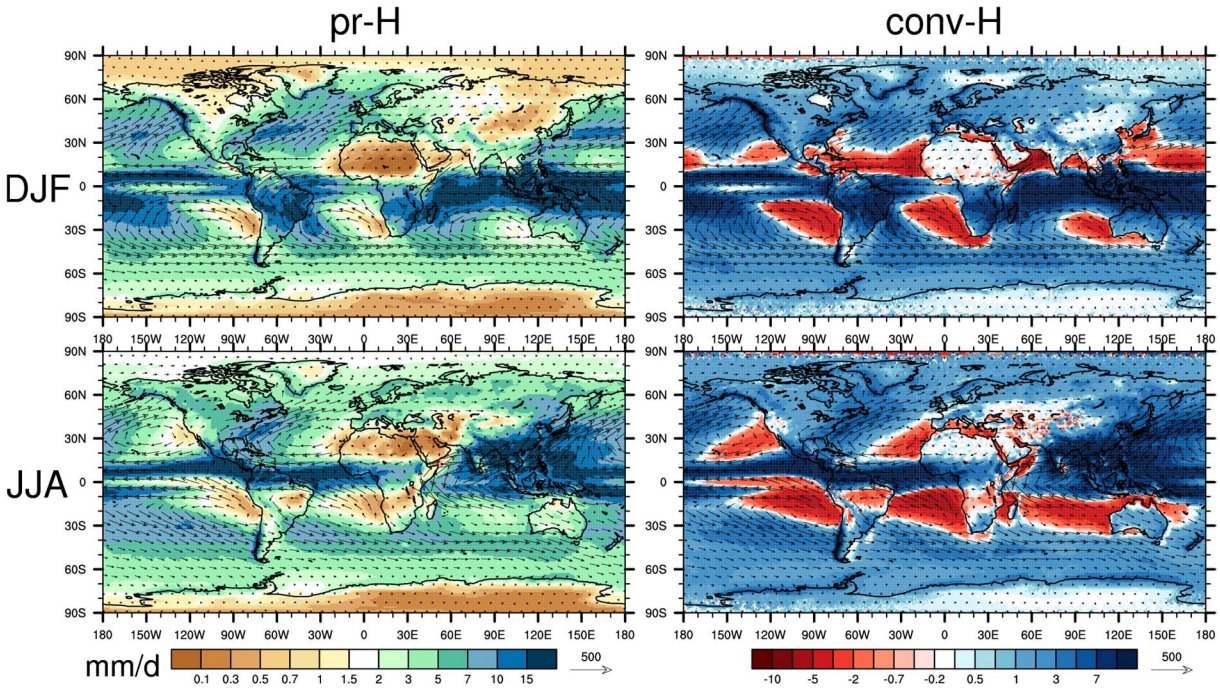

FIGURE 4 As Figure 3, but for months with top decile of rainfall (H), calculated at each grid point.

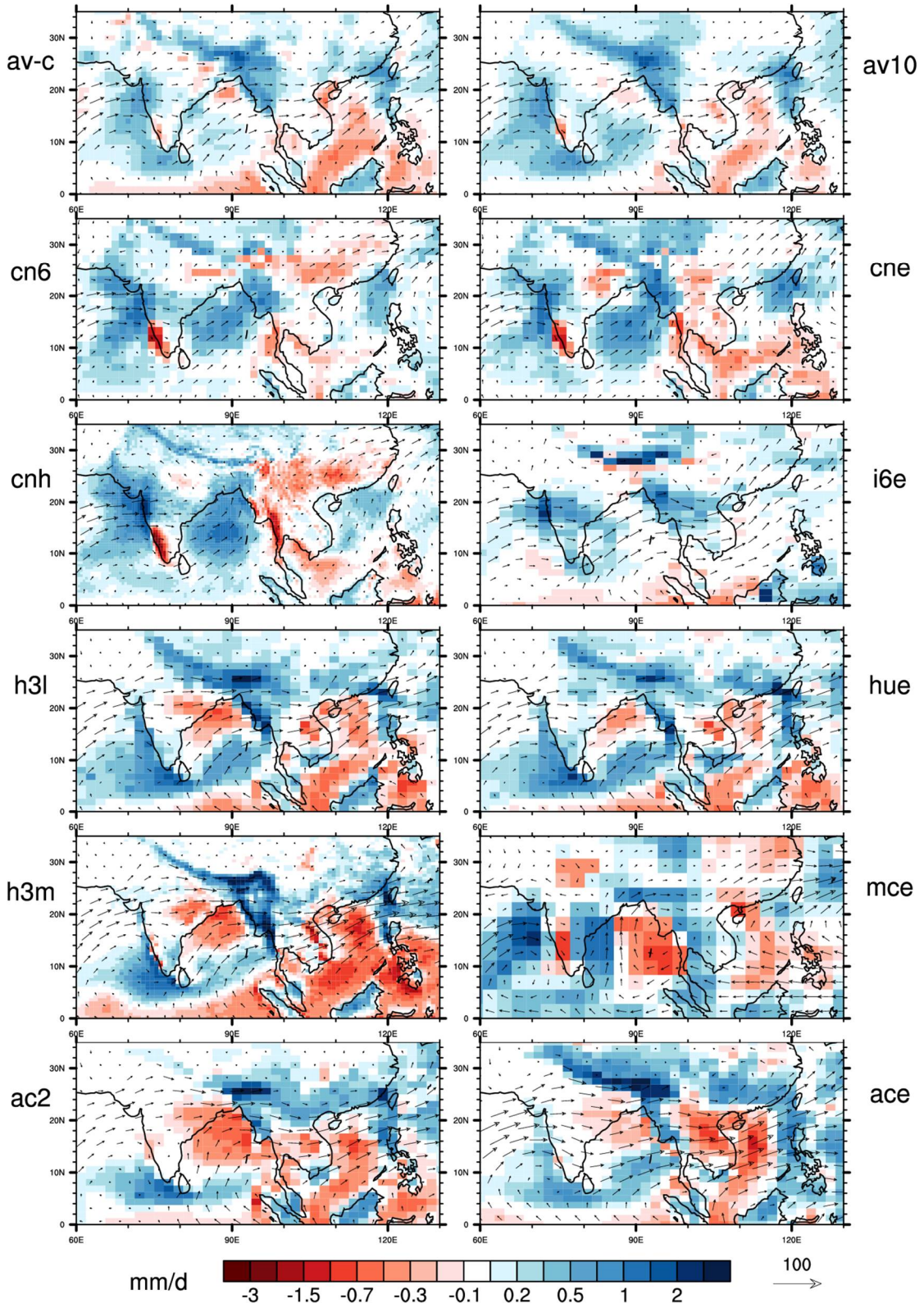

FIGURE 5 Standardized change (or change per degree of global warming) from ten models for the Southern Asia summer monsoon. Other than the top left, the plots show JJA fields for precipitation, in mm d^{-1}, with moisture flux as a vector, with the reference vector being 100 kg m^{-1} s^{-1}. The top row shows the av10 fields, but with pr replaced by convergence in the left plot. Vectors are shown as for Fig. 1.

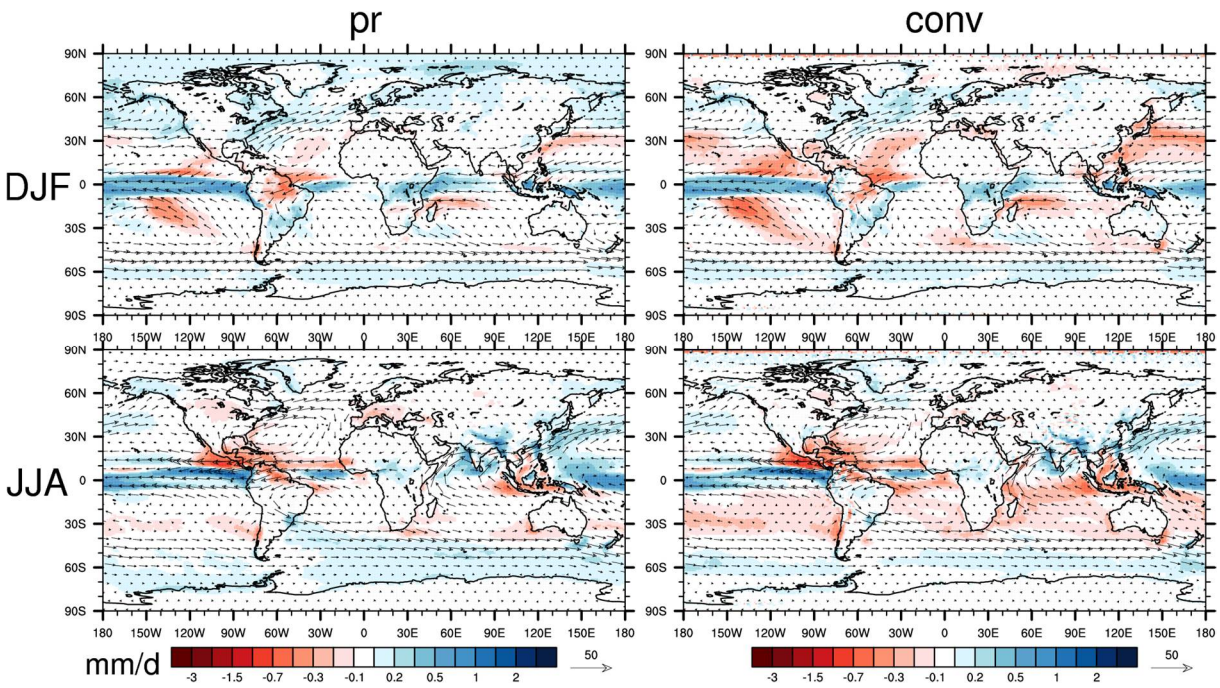

FIGURE 6 As Figure 3, but all quantities are standardized change. Note the smaller reference vector, and here the scales are the same for each variable.

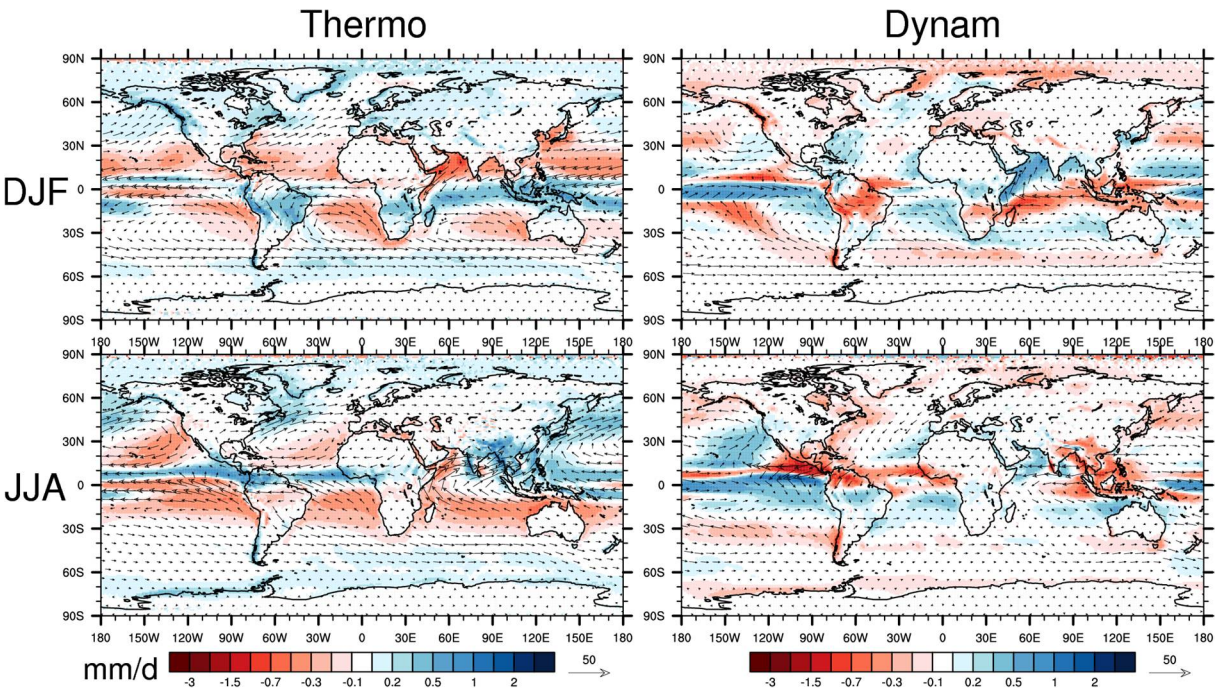

FIGURE 7 As Figure 6 (right) but with the fields replaced by two components of change in convergence and flux, (left) thermodynamic component (using fractional change of prw) and (right) dynamic component, as the residual change.

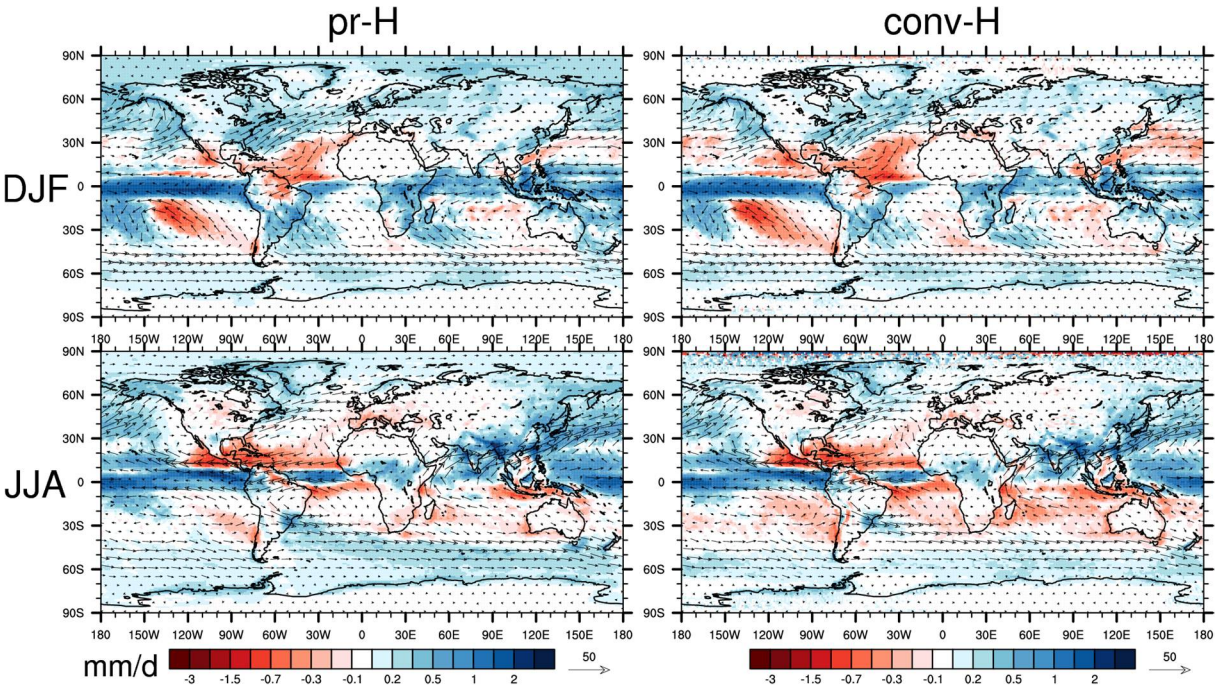

FIGURE 8 As Figure 6, for H composites, but standardized change.

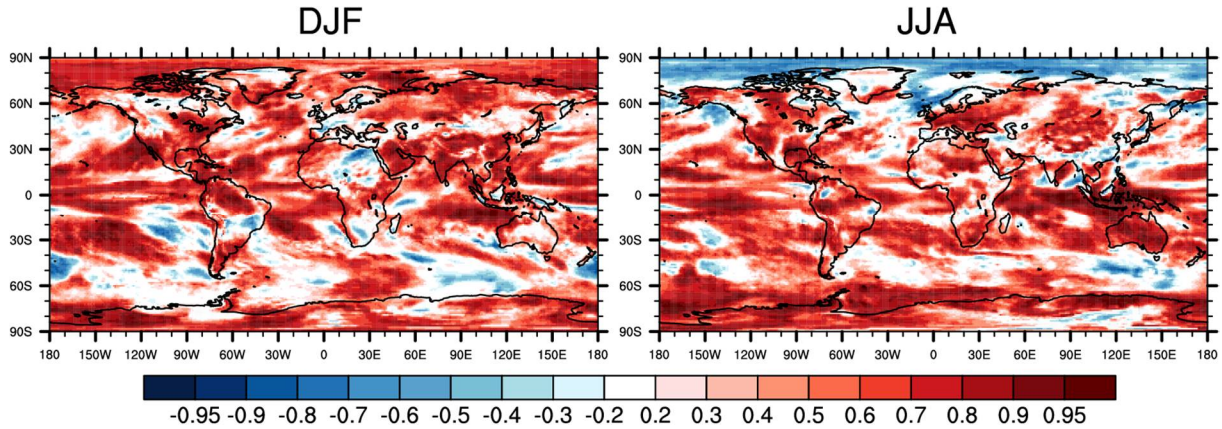

FIGURE 9 Correlations (*r*) between percentage changes in pr and prw, across the ten-model ensemble, left for DJF, right JJA. The values are calculated at each one-degree grid point, after interpolation of the model fields.